

estimates of the overall galaxy merger rate, but it should be a fair estimate unless there is a correlation between the presence of the radio source and the population of galaxies undergoing mergers. There are indeed reasons to believe that there may be such a correlation (23) and, more speculatively, the black hole coalescence itself may be the trigger for the active galaxy phenomenon. Any such correlation would decrease the implied merger rate for the galaxy population as a whole, but rates of  $\sim 1 \text{ Gy}^{-1}$  are typical of those inferred for galaxies in dense regions or groups (24). Our result should motivate more detailed studies of galaxy mergers in the hope of demonstrating that binary SBHs can indeed avoid "stalling" and go on to rapid coalescence.

If the coalescence rate of binary SBHs is comparable to the galaxy merger rate, then the binary separation must be able to drop from  $\sim 1$  to  $\sim 0.01 \text{ pc}$  in a time shorter than  $\sim 1 \text{ Gy}$ . The predicted event rate for gravitational wave interferometers should then be about equal to the integrated galaxy merger rate out to a redshift  $z \approx 5$ , implying a time between detections of  $\sim 1 \text{ year}$  (25).

# References and Notes

1. P. L. Bender, in *Gravitational Waves*, I. Ciufolini et al., Eds. (Institute of Physics Publishing, Bristol, UK, 2001), p. 115–133.
2. M. Milosavljevic, D. Merritt, *Astrophys. J.* **563**, 34 (2001).
3. E. E. Flanagan, S. A. Hughes, *Phys. Rev. D* **57**, 4535 (1998).
4. J. M. Bardeen, *Nature* **226**, 64 (1970).
5. L. E. Kidder, C. M. Will, A. G. Wiseman, *Phys. Rev. D* **47**, 3281 (1993).
6. J. Baker, M. Campanelli, C. O. Lousto, R. Takahashi, *astro-ph/0202469* (2002).
7. J. M. Bardeen, J. A. Petterson, *Astrophys. J.* **195**, L65 (1975).
8. M. J. Rees, *Nature* **275**, 516 (1978).
9. M. C. Begelman, R. D. Blandford, M. J. Rees, *Rev. Mod. Phys.* **56**, 255 (1984).
10. C. Auriemma et al., *Astron. Astrophys.* **57**, 41 (1977).
11. R. D. Ekers, R. Fanti, C. Lari, P. Parma, *Nature* **276**, 588 (1978).
12. M. Murgia et al., *Astron. Astrophys.* **380**, 102 (2001).
13. J. E. Pringle, *Mon. Not. R. Astron. Soc.* **281**, 357 (1996).
14. D. Merritt, F. Cruz, *Astrophys. J.* **551**, L4a (2001).
15. J. P. Leahy, P. Parma, in *Extragalactic Radio Sources. From Beams to Jets*, J. Roland et al., Eds. (Cambridge Univ. Press, Cambridge, UK, 1992), p. 307–308.
16. The Fanaroff-Riley types I and II are a morphological classification defined by the degree of edge-brightening in the radio lobes [see B. Fanaroff, J. Riley, *Mon. Not. R. Astron. Soc.* **167**, 31P (1974)].
17. S. Wilson, E. J. M. Colbert, *Astrophys. J.* **438**, 62 (1995).
18. A minor merger is one in which the infalling galaxy has a mass that is 30% or less that of the larger galaxy.
19. D. Merritt, L. Ferrarese, *Mon. Not. R. Astron. Soc.* **320**, L30 (2001).
20. J. Dennett-Thorpe et al., *Mon. Not. R. Astron. Soc.* **330**, 609 (2002).
21. D. Merritt, in *XVth IAP Meeting Dynamics of Galaxies: From the Early Universe to the Present*, Institut d'Astrophysique de Paris, 9 to 13 July 1999, F. Combes et al., Eds. (Astronomical Society of the Pacific, San Francisco, 2000), vol. 197, p. 221–230.
22. C. P. O'Dea, R. N. Owen, *Astron. J.* **90**, 954 (1985).
23. T. M. Heckman et al. *Astrophys. J.* **311**, 526 (1986).

24. R. G. Carlberg et al. *Astrophys. J.* **532**, L1 (2000).
25. M. G. Haehnel, in *Laser Interferometer Space Antenna*, Jet Propulsion Laboratory, Pasadena, CA, 10 to 15 July 1998, W. M. Folkner, Ed. (American Institute of Physics, Woodbury, NY, 1998), vol. 456, p. 45.
26. M. Murgia, thesis, University of Bologna (2000).
27. U. Klein, K.-H. Mack, L. Gregorini, P. Parma, *Astron. Astrophys.* **303**, 427 (1995).
28. J. P. Leahy, A. G. Williams, *Mon. Not. R. Astron. Soc.* **210**, 929 (1984).
29. J. Dennett-Thorpe, A. H. Bridle, R. A. Laing, P. A. G. Scheuer, *Mon. Not. R. Astron. Soc.* **304**, 27 (1999).

30. P. Leahy kindly allowed us to reproduce the Leahy and Parma catalog of X-shaped radio sources (15) in Table 1. We thank him, L. Ferrarese, S. Hughes, M. Milosavljevic, and C. O'Dea for useful discussions. Supported by the NSF through grant 4-21911, NASA through grants 4-21904 and NAG5-8693, and the Miller Institute at the University of California at Berkeley.

4 June 2002; accepted 17 July 2002

Published online 1 August 2002;

10.1126/science.1074688

Include this information when citing this paper.

## Current Rectification by Pauli Exclusion in a Weakly Coupled Double Quantum Dot System

K. Ono,<sup>1</sup> D. G. Austing,<sup>2,3</sup> Y. Tokura,<sup>2</sup> S. Tarucha<sup>1,2,4\*</sup>

We observe spin blockade due to Pauli exclusion in the tunneling characteristics of a coupled quantum dot system when two same-spin electrons occupy the lowest energy state in each dot. Spin blockade only occurs in one bias direction when there is asymmetry in the electron population of the two dots, leading to current rectification. We induce the collapse of the spin blockade by applying a magnetic field to open up a new spin-triplet current-carrying channel.

Current flow through an electronic system between contact leads (source and drain leads) is determined by the transition rates between the source lead and the drain lead, via states in the electronic system. When inversion symmetry is absent in the system, the electrical current can provide bias-dependent rectification. This was first suggested for a single molecule with appropriately configured molecular orbitals by Aviram and Ratner (1) many years ago, and very recently for multiple dots suffering from the Coulomb blockade effect (2). In both of these cases, the rectifying effect depends on bias-dependent transition rates and is characterized by irreversible trapping in a state from which current can no longer proceed.

Transition rates in electronic systems depend in general on the Pauli exclusion principle, which prevents two electrons of parallel spin from occupying a single spatial orbital. Observation of the Pauli effect in condensed matter systems depends, however, on low temperatures and reduced dimensions such that the energy spacing of states at the

Fermi level is comparable to, or larger than, the thermal energy. One recently observed manifestation of this exchange (i.e., Pauli exclusion) effect in one-dimensional (1D) systems is the suppression of the current noise due to anti-bunching of electrons (3, 4). Here, we show that in transport through a series of 0D sites, with symmetry under inversion appropriately broken, the Pauli effect, in combination with the Coulomb blockade, can be used to block current altogether in one direction while permitting it to flow in the opposite direction, thereby realizing a fully controllable spin-Coulomb rectifier.

Quantum dots are often referred to as artificial atoms because the electrons inside are well confined in 0D states and the electronic properties are analogous to those of real atoms (5, 6). The electronic configuration and the number of electrons in the quantum dot are parameters that can be easily manipulated (6–8). A quantum dot containing one electron in a single orbital state is just like a hydrogen atom. We use two weakly coupled hydrogen-like quantum dots to construct a diatomic molecule that forms the two-electron two-site system. We can then observe the consequences of Pauli exclusion directly on single-electron tunneling via the two-electron states.

Suppose we have two sites, site 1 and site 2, weakly coupled together, and one electron is permanently localized on site 2 (Fig. 1A). Now consider transport of a second electron through the system between two contact leads. The number of electrons on site 1 ( $N_1$ ), varies between 0 and 1 (1 and 2). An

<sup>1</sup>Department of Physics, University of Tokyo, Hongo, Bunkyo-ku, Tokyo 113–0033, Japan. <sup>2</sup>Nippon Telegraph and Telephone Basic Research Laboratories, NTT Corporation, Atsugi-shi, Kanagawa 243–0198, Japan. <sup>3</sup>Institute for Microstructural Sciences M23A, National Research Council of Canada, Ottawa, Ontario K1A 0R6, Canada. <sup>4</sup>Exploratory Research for Advanced Technology Mesoscopic Correlation Project, Japan Science and Technology, Atsugi-shi, Kanagawa 243–0198, Japan.

\*To whom correspondence should be addressed. E-mail: tarucha@phys.s.u-tokyo.ac.jp

electron can only be transported through the system when the transition between the two-electron states  $(N_1, N_2) = (0, 2)$  and  $(1, 1)$  is allowed. This condition is met when the necessary energy cost to add one more electron to the system is compensated for by the action of a nearby plunger gate voltage, or the voltage between the leads, which is a familiar single-electron charging phenomenon (5).

Crucially, spin effects also markedly influence electron transport. Because the tunnel coupling between the two sites is sufficiently weak, the  $(N_1, N_2) = (1, 1)$  spin-singlet and spin-triplet states are practically degenerate (9). Additionally, for  $(N_1, N_2) = (0, 2)$ , only a spin singlet is permitted because of Pauli exclusion. Therefore, electron transport is only allowed for a channel made from the  $(1, 1)$  and  $(0, 2)$  singlet states. This always holds true for reverse bias when the chemical potential of the left lead,  $\mu_\ell$ , nearest site 1, is lower than that of the right lead,  $\mu_r$ , nearest site 2, because only an antiparallel spin electron can be injected onto site 2 from the right lead (Fig. 1A). On the other hand, for forward bias,  $\mu_\ell > \mu_r$ , either the  $(1, 1)$  singlet or triplet can be populated with more or less the same probability by injection of an electron onto site 1 from the left lead. If the  $(1, 1)$  singlet is populated, a single-electron tunneling current can flow through the singlet state. Once the triplet is populated, however, subsequent electron transfer from site 1 to 2 is blocked by Pauli exclusion. Note that an electron arriving on site 1 usually cannot go back to the left lead because of the fast relaxation of the hole state left behind in the lead (10). Thus the  $(1, 1)$  triplet will sooner or later be occupied on a time scale sufficiently longer than the electron tunneling time between the leads, and this should lead to clear current suppression, for example, in dc measurement. Because this blockade is due to spin and not charge, we hereafter refer to this process as "spin blockade," and this provides current rectification. Blockade of single-electron transport associated with spin has been reported for single-dot (11–13) and double-dot (14, 15) systems. In most of these cases, blockade appears only when the difference in the total spin between the  $N$  and  $N + 1$  electron ground states (GSs) is greater than  $1/2$ . Such a large difference cannot be made up by single-electron tunneling events, but this itself is not related to Pauli exclusion.

Our double-dot device is made by vertically coupling two circular quantum dots that are located between two contact leads called the source and drain (Fig. 1B) (16, 17). The lateral confinement in each dot imposed by the surrounding Schottky gate is well approximated by a 2D harmonic potential (6, 18). A quantum dot with such a potential has atom-like electronic properties: shells composed of  $1s, 2p, 3s, 3d, \dots$  orbitals and the filling of

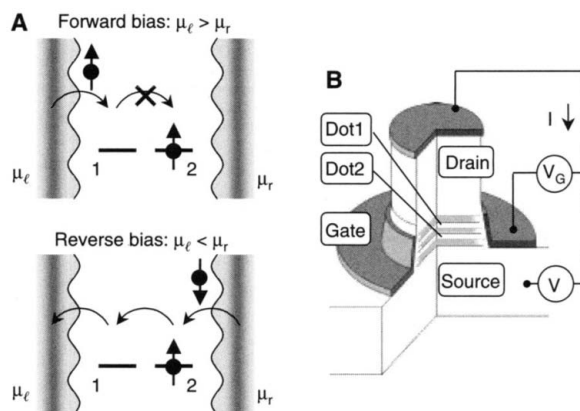
near degenerate states in accordance with Hund's first rule (6, 7). The typical characteristic energy,  $\hbar\omega_0$ , of the lateral confinement in each dot is about 4 meV for the lowest  $1s$  orbital state (18). Located  $\hbar\omega_0$  above is the excited  $2p$  orbital state. In our vertical device configuration, the total number of electrons in the whole double-dot system,  $N (= N_1 + N_2)$ , can be varied one-by-one as a function of gate voltage,  $V_G$ , starting from  $N = 0$  (6, 17). Here, we label the two dots "dot 1" and "dot 2," and they correspond to site 1 and site 2 in Fig. 1A, respectively. Similarly,  $N_1$  ( $N_2$ ) is now the number of electrons in dot 1 (dot 2). The transmission coefficients for all the tunnel barriers (dot-contact lead and dot-dot) are sufficiently weak that electron transport can be discussed just in terms of sequential tunneling between the source and drain.

The general situation of Fig. 1A can be reproduced in our structure (see Fig. 2A, potential diagrams) if there is an appropriate potential offset,  $2\delta$ , between the two quantum dots at zero source-drain voltage,  $V = 0$  V (19, 20). Then, just one electron is trapped in the  $1s$  orbital state of dot 2, and the two-electron GS is either  $(N_1, N_2) = (1, 1)$  or  $(0, 2)$ . For  $(1, 1)$ , the singlet and triplet states are nearly degenerate because the coupling between the two dots is very weak (9). For  $(0, 2)$ , only the singlet GS is initially relevant. A  $(0, 2)$  triplet excited state (ES) can be formed by putting two parallel spin electrons in the  $1s$  and  $2p$  states in dot 2. However, its energy is normally much higher than that of the  $(1, 1)$  and  $(0, 2)$  GS, so it does not influence the transport in our discussion for the moment. When viewing Fig. 1A, we can see that electrons can be transported by the  $(0, 2)$

and  $(1, 1)$  singlet states for reverse bias, whereas for forward bias, the  $(1, 1)$  triplet can be populated, leading to the blockade of electron transport. We now define the electrochemical potential of the  $(N_1, N_2)$  GS to be  $\mu(N_1, N_2)$  and the chemical potential of the source (drain) lead to be  $\mu_s$  ( $\mu_d$ ). Spin blockade in Fig. 1A can appear when electrons are injected from the drain to the  $(1, 1)$  triplet in the nonlinear transport (21). We assume that spin is conserved in the electron tunneling throughout our double-dot system and that there are no spin flips on a time scale sufficiently longer than the electron tunneling time. This condition actually holds for our experiments, which we will explain later.

We measure the dc current,  $I$ , flowing vertically through the two dots as a function of  $V_G$  and  $V$  to study the linear and nonlinear electron transport.  $V_G$  and  $V$ , respectively, are used to change the electrostatic potential of the two dots together, and the potential offset between the two dots. By adjusting these voltages and using a double-dot sample with an appropriate potential offset  $2\delta$  (19), we can realize the situation in Fig. 1A.  $dI/dV - V_G$  measured for small  $V$  ( $\sim 0$  V) shows clear Coulomb oscillation peaks (Fig. 2A, lower right inset).  $N$  increases one-by-one, starting from  $N = 0$  every time a current peak is crossed as  $V_G$  is made more positive. The first peak (X) is very small but definitely present at  $V_G \sim -2$  V, and this indicates transport through the double-dot system for  $N$  fluctuating between 0 and 1. The second peak (P) and the third peak (Q) are much larger. This implies that tunneling is elastic between the source and drain leads for  $N = 1 \leftrightarrow 2$  and  $2 \leftrightarrow 3$ . However, because of the potential offset between the two dots, this is not the case

**Fig. 1.** Model for rectification of the single-electron tunneling current by the Pauli effect. (A) Electron transport through a generic two-site system with one electron trapped permanently on site 2. For reverse bias, a transport channel through two-electron singlet states is always available; however, for sufficiently large forward bias a triplet state with an electron on each site is sooner or later occupied. Further electron transport is then blocked due to Pauli exclusion. (B) Schematic of the double-dot device (16–18). The specific device we discuss is a 0.6- $\mu\text{m}$  cylindrical mesa made from an AlGaAs (8 nm)/InGaAs (12 nm)/AlGaAs (6 nm)/InGaAs (12 nm)/AlGaAs (8 nm) triple barrier structure located between the n-GaAs source and drain leads. Both quantum dots are strongly confined vertically by heterostructure barriers and softly confined laterally by an approximate 2D harmonic potential imposed by the common Schottky gate wrapped around the mesa. The tunnel coupling energy between two dots is estimated to be 0.3 meV (17). This is much smaller than the 2D harmonic potential energy ( $\hbar\omega_0 \sim 4$  meV) and the charging energy for each dot ( $U \sim 4$  meV). The conditions in (A) are achieved by adjusting the source-drain voltage,  $V$ , and the gate voltage,  $V_G$ , in the presence of an appropriate potential offset between the two dots.



for  $N = 0 \leftrightarrow 1$ . Electrons must tunnel through the lowest state in dot 2, but since there is no available state for tunneling in dot 1, second-order tunneling through dot 1 is necessary (22). We then study nonlinear transport through the two-electron states by measuring the  $I$ - $V$  for  $V_G$  fixed at the second Coulomb oscillation peak (Fig. 2A, main curve). The data reveal a large, nearly constant  $dI/dV$  at  $V \sim 0$  V for both bias polarities, and this is due to elastic tunneling in the linear response regime. Tunneling here occurs via the (1,1)

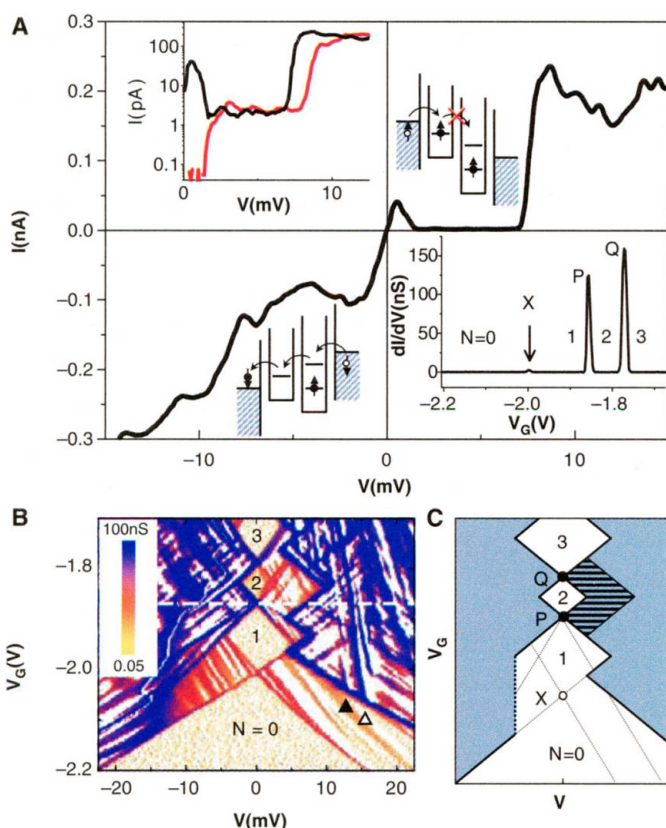
and (0,2) singlet states, which are aligned at  $V \sim 0$  V when we take into account the effect of the potential offset  $2\delta$ . For  $|V| \geq 1$  mV, transport is nonlinear (see potential diagrams in Fig. 2A). The current is clearly suppressed in forward bias because of spin blockade, whereas a large current still flows in reverse bias because of inelastic tunneling via the singlet states. The spin blockade is lifted for  $V > 7$  mV when an electron can be ejected from the lowest state of dot 2 to the source. The spin blockade is further confirmed from

measurements of nonlinear transport for a wide range of  $V_G$  values (Fig. 2B).

The spin blockade should appear everywhere the forward bias situation of Fig. 1A is satisfied in the  $(V, V_G)$  plane. Such a region is indeed observed in the experimental data of  $dI/dV$  versus  $V$  and  $V_G$ , which is plotted on a logarithmic scale in Fig. 2B. The central three diamond-shaped regions of  $dI/dV \sim 0$  siemens identify the  $N = 1$  to 3 regions of Coulomb blockade. Note that the diamonds touch each other at  $V \sim 0$  V for  $V_G$  values corresponding to the Coulomb oscillation peaks in Fig. 2A. Application of a sufficiently large  $V$  will usually lead to the lifting of Coulomb blockade by the addition of an electron to dot 1 (dot 2) from the drain (source), or the removal of an electron from dot 1 (dot 2) to the drain (source). At the threshold for lifting the Coulomb blockade, a large inelastic tunneling current (or large  $dI/dV$ ) appears when two states, one for each dot, are present between  $\mu_e$  and  $\mu_r$ . This holds true for all of the  $N > 1$  regions of Coulomb blockade, but only partly for the  $N = 1$  region. This is because the presence of the potential offset will mean only one state can lie between  $\mu_e$  and  $\mu_r$ . In addition, we can also see that the right boundary of the  $N = 2$  Coulomb blockade diamond is marked by a weak  $dI/dV$  threshold. Located to the right is an extended region of small  $dI/dV$ . This is the region where nonlinear transport involving two-electron states occurs. The (1,1) (singlet and triplet) and (0,2) (singlet and triplet) states are all located between  $\mu_e$  and  $\mu_r$  of the contact leads, and so the conductance suppression is assigned to the spin blockade (see Fig. 2A, forward bias potential diagram). The spin blockade is lifted when the forward bias is sufficiently large that the electron initially trapped in dot 2 is ejected to the source, or one more electron is injected into dot 1 from the drain. The former (later) is given by the condition  $\mu(0,1) \geq \mu_r$  ( $\mu_e \geq \mu(2,1)$ ), which determines the lower right (upper right) boundary of the spin blockade region. Note that to the left of the  $N = 2$  Coulomb blockade diamond, there is no such current suppression, because the transition  $(0,2) \rightarrow (1,1)$  via the singlet states is always allowed (see Fig. 2A, reverse bias potential diagram).

In Fig. 2C, with the aid of a simple model, we reproduce important features in the experimental data of Fig. 2B (23). The bold lines enclosing the diamond-shaped regions indicate the thresholds for lifting Coulomb blockade in both dots. The faint dotted lines inside and below the  $N = 1$  Coulomb diamond indicate threshold values due to the second-order tunneling (24). The spin blockade region is located to the right of the  $N = 2$  Coulomb diamond. In addition, the potential offset  $2\delta$  can be "tuned out" to allow elastic tunneling

**Fig. 2.** Spin blockade of single-electron tunneling current in a weakly coupled double-dot system. (A) Coulomb oscillations in  $dI/dV$  versus  $V_G$  curve for small  $V$  ( $\sim 0$  V) (lower right inset) and  $I$  versus  $V$  curve measured for  $V_G$  fixed at the second Coulomb oscillation peak labeled P. All data are taken at an effective electron temperature of about 0.2 K, and about 10% of the applied voltage  $V$  is dropped between the two dots. The second and third Coulomb oscillation peaks (P and Q) are large because of elastic tunneling throughout the system, whereas the first peak (X) is very small because of second-order tunneling through dot 1. The main  $I$ - $V$  curve shows electron transport through the singlet states in the linear response region for  $|V| < 1$  mV. For nonlinear transport in forward bias, the spin blockade region associated with the formation of the (1,1) triplet is for  $V$  from 1 to 7 mV. The two potential diagrams illustrate the situations for spin blockade in forward bias and continuous electron transport via the singlet states in reverse bias. The upper left inset shows magnified plots of  $I$  versus  $V$  for  $V_G$  fixed at peak P (black curve) and in the middle between the peaks P and Q (red curve) on a logarithmic scale. Both curves show current suppression ( $I \sim 2$  pA) due to spin blockade. In the vicinity of  $V = 0$  V, the red curve shows strong current suppression due to Coulomb blockade. (B) Differential conductance,  $dI/dV$ , as a function of  $V$  and  $V_G$  on a logarithmic scale (the darker the color, the larger the value of  $dI/dV$ , and negative  $dI/dV$  is set to white). The red and blue lines identify the presence of current steps on the order of 1 pA and 100 pA, respectively. Each Coulomb blockade region is clearly bound by lines marking the thresholds for the lifting of Coulomb blockade. To the right of the  $N = 2$  Coulomb blockade region there is a region of suppressed  $dI/dV$  due to spin blockade. The section identified by the horizontal dashed line is derived from the main  $I$ - $V$  curve in Fig. 2A.  $\blacktriangle$  and  $\triangle$  mark resonance between the  $1s$  (dot 1) and  $2p^+$  and  $2p^-$  (dot 2) states, respectively (see Fig. 3, A and B). (C) Key nonlinear transport features recovered from a simple model of the present sample. For simplicity we set  $U_{12} = (1/2)U$ , where  $U$  and  $U_{12}$ , respectively, are the charging energy for each dot, and electrostatic coupling energy between the two dots (22, 32), and also  $2\delta = U - U_{12}$ .  $U$ ,  $U_{12}$ , and  $2\delta$  are all assumed to be independent of the number of electrons. The voltage drop between the source and drain is distributed equally across all three tunnel barriers. The points X, P, and Q correspond to the first, second, and third Coulomb oscillation peaks, respectively, in (A). The bold solid lines indicate the threshold for the lifting of Coulomb blockade in both dots. The hatched region to the right of the  $N_1 + N_2 = 2$  Coulomb blockade region is the spin blockade region. The faint dotted lines indicate the threshold for the lifting of the  $N = 1$  Coulomb blockade region due to second-order tunneling (24). The vertical dotted line in reverse bias indicates elastic tunneling of electrons through the lowest state in each dot.



of electrons through the (1,0) and (0,1) states by application of an appropriate reverse bias. This occurs along the vertical dashed line. Figure 2C reproduces quite well the shape and size of all the important features in Fig. 2B, and this allows us to be confident that we correctly identify the measured spin blockade region.

The main  $I$ - $V$  curve in Fig. 2A is actually used to make the data section at  $V_G = -1.854$  V in Fig. 2B (horizontal white dashed line). From the level of the current in the spin blockade region (black curve in the upper left inset to Fig. 2A), we estimate the lifetime of the spin triplet to be  $e/I \sim 100$  ns. This is markedly longer than the time taken for just single-electron inelastic tunneling between the contact leads ( $e/I \sim 1.6$  ns) obtained from the current level for  $V < -1$  mV. From Fig. 2B we also find that the magnitude of the current in the spin blockade region is more or less the same as that observed in the vicinity of the lower part of the  $N = 1$  Coulomb blockade region. This suggests that the current in the spin blockade region due to the decay of the (1,1) triplet state is also caused by second-order tunneling processes (25) and that the intrinsic spin-flip relaxation time is longer than 100 ns. An even longer relaxation time for spin has recently been reported for a single quantum dot (26). The upper left inset to Fig. 2A also shows the  $I$  versus  $V$  curve that cuts across the center of the  $N = 2$  Coulomb blockade region (red curve). Here, the current level in the spin blockade region is the same as that for the black curve, but the current level is much lower in the region of Coulomb blockade ( $<100$

fA). This clearly demonstrates that current leakage is negligible in our system.

To explore further the spin blockade region in Fig. 2, A and B, we study the influence of a magnetic field ( $B$  field) applied parallel to the current flowing through the two dots. In our model, spin blockade in forward bias can be lifted if a  $(N_1, N_2) = (0, 2)$  triplet is available, and it can be made lower in energy than the (1,1) triplet (Fig. 3A). Then, a spin-triplet channel is opened and current can flow. The (0,2) triplet at low  $B$  field is the ES with two parallel spin electrons in dot 2, one in the  $1s$  state and the other in the  $2p$  state. At  $B = 0$  T, the  $2p$  single-particle state has a twofold orbital degeneracy. The  $2p^+$  and  $2p^-$  states have orbital angular momentum quantum numbers of  $+1$  and  $-1$ , respectively, due to the rotational symmetry in the lateral confinement. When the  $B$  field is initially increased, the  $2p^+$  and  $2p^-$  states split apart, and so the energy of the  $2p^+$  state approaches that of the  $1s$  state. In addition, the Coulomb energy of the two-electron states is increased due to magnetic confinement of the wave functions, but it occurs at a slower rate for the (0,2) triplet than for both the (1,1) triplet and (0,2) singlet, because the  $2p$  state is more spatially extended than the  $1s$  state. Therefore, the (0,2) triplet becomes energetically favored relative to the other two-electron states (27). To track the  $B$  field-induced change in energy of the (0,2) triplet relative to the (1,1) triplet, we investigate the related resonance, which gives rise to a current peak in forward bias. The  $1s$ - $2p^+$  ( $1s$ - $2p^-$ ) resonance peak is identified by the line labeled  $\blacktriangle$  ( $\nabla$ ) at  $B = 0$  T in Fig. 2B (28, 29). The fact that these two resonance

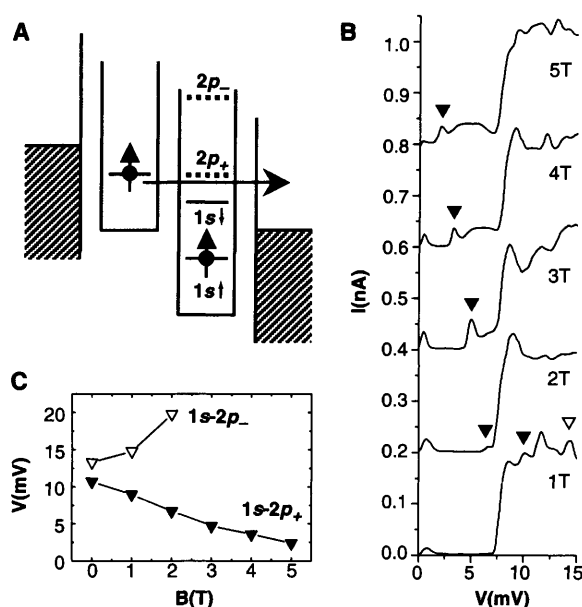
lines are slightly separated is probably due to small asymmetry in the lateral confinement. Fig. 3B shows the  $B$  field-induced downshift of the  $1s$ - $2p^+$  resonance, which is identified by the current peak labeled  $\blacktriangle$  in  $I$ - $V$  curves that cut across the spin blockade region. In Fig. 3C, the plotted shift of both the  $1s$ - $2p^+$  and  $1s$ - $2p^-$  resonances reflects directly the expected trend for  $1s$  and  $2p$  Fock-Darwin states (6, 29). As the  $B$  field is increased toward 5 T, the  $1s$ - $2p^+$  current peak approaches the  $V = 0$  V axis as it progressively enters the spin blockade region. Spin blockade is then lifted, and we can see enhanced current on and to the right of the current peak. We note that for plots like Fig. 2B, but for  $B \geq 5$  T, part of the  $1s$ - $2p^+$  resonance line actually enters the  $N = 2$  Coulomb blockade region and immediately disappears. This  $B$  field signature also clearly demonstrates that the spin blockade observed in Fig. 2, A and B, is spin-related rather than charge-related.

Our experiments on a weakly coupled double quantum dot system reveal directly the importance of Pauli exclusion on spin transport. The observed current rectification has possible applications to spin memories, filters, and transistors.

## References and Notes

- See, for example, C. Joachim, J. K. Gimzewski, A. Aviram, *Nature* **408**, 541 (2000) and references therein.
- M. Stopa, *Phys. Rev. Lett.* **88**, 146802 (2002).
- A. Kumar, L. Saminadayer, D. C. Glattli, Y. Jin, E. Etienne, *Phys. Rev. Lett.* **76**, 2778 (1996).
- R. C. Liu, B. Odorn, Y. Yamamoto, S. Tarucha, *Nature* **391**, 263 (1998).
- For a review on quantum dots, see L. P. Kouwenhoven et al., in *Mesoscopic Electron Transport*, L. L. Sohn, G. Schon, L. P. Kouwenhoven, Eds. (Kluwer, Dordrecht, Netherlands, Series E345, 1997).
- S. Tarucha, D. G. Austing, T. Honda, R. J. van der Hage, L. P. Kouwenhoven, *Phys. Rev. Lett.* **77**, 3613 (1996).
- S. Tarucha, D. G. Austing, Y. Tokura, W. G. van der Wiel, L. P. Kouwenhoven, *Phys. Rev. Lett.* **84**, 2485 (2000).
- M. Ciorga et al., *Phys. Rev. Lett.* **88**, 256804 (2002).
- The  $(N_1, N_2) = (1, 1)$  singlet and triplet states are only separated by the Heisenberg exchange energy, which is much smaller than other energy scales considered here.
- When the forward bias is sufficiently small, as compared to the coupling energy between the left lead and site 1, or to the effective electron temperature, the electron on site 1 of the (1,1) triplet can go back to the left lead, in which case current suppression does not occur. This is the case only for linear transport near zero bias where we should expect to observe a single-electron tunneling current.
- D. Weimann, H. Hausler, B. Kramer, *Phys. Rev. Lett.* **74**, 984 (1995).
- Y. Tanaka, H. Akera, *Phys. Rev. B* **53**, 3091 (1996).
- M. Ciorga et al., *Phys. Rev. B* **61**, R16315 (2000).
- H. Imamura, H. Aoki, P. A. Maksym, *Phys. Rev. B* **57**, R4259 (1998).
- Y. Tokura, D. G. Austing, S. Tarucha, *J. Phys.: Condens. Matter* **11**, 6023 (1999).
- D. G. Austing, T. Honda, S. Tarucha, *Semicond. Sci. Technol.* **11**, 388 (1996).
- D. G. Austing et al., *Physica B*, **249–251**, 206 (1998).
- S. Amaha et al., *Solid State Comm.* **119**, 183 (2001).
- This potential offset,  $2\delta$ , ranging from  $\sim 0.5$  to a few meV, has been observed in all of our double-dot samples and is probably due to a small decrease in the effective electron density in the cylindrical mesa

**Fig. 3.** Collapse of spin blockade induced by a magnetic field. (A) Schematic potential diagram showing how spin blockade is lifted by the  $B$  field-induced lowering of a  $2p$  state in dot 2. As the  $B$  field is initially increased, the two (ideally degenerate)  $2p$  states split into the  $2p^+$  and  $2p^-$  states, and the  $2p^+$  state moves down toward alignment with the lowest  $1s$  state in dot 1. (B)  $B$  field-induced shift of the  $1s$ - $2p^+$  and  $1s$ - $2p^-$  resonance peaks labeled  $\blacktriangle$  and  $\nabla$ , respectively, in the  $I$ - $V$ , which cuts across the spin blockade region (horizontal dashed line in Fig. 2B). When the resonance peak enters the spin blockade region for  $B \geq 2$  T, spin blockade is lifted on and to the right of the resonance peak. The  $I$ - $V$  curves are vertically offset for clarity. (C) Evolution of the  $1s$ - $2p^+$  ( $\blacktriangle$ ) and  $1s$ - $2p^-$  ( $\nabla$ ) resonance peak positions with  $B$  field. As the  $B$  field is initially increased, the  $1s$ - $2p^+$  ( $1s$ - $2p^-$ ) resonance peak moves down (up).



- just above the two dots relative to that below (20). We select here a double-dot sample where  $2\delta \sim U - U_{12}$ , so we can realize the condition  $\mu(1,1) = \mu(0,2)$  at  $V = 0$  V.
20. M. Pi *et al.*, *Phys. Rev. Lett.* **67**, 066801 (2001).
21. The precise condition is that  $\mu_e > \mu(1,1) \geq \mu(0,2) > \mu_v$ .
22. D. V. Averin, Yu. V. Nazarov, in *Coulomb Blockade Phenomena in Nanostructures*, H. Grabert, M. H. Devoret, Eds. (Plenum Press and NATO Scientific Affairs Division, New York, 1992), pp. 217–247.
23. Details will be described elsewhere.
24. For  $N = 1$ , the Coulomb blockade region is initially partially lifted with  $V$  because of second-order tunneling when only one state of either dot 1 or 2 is between  $\mu_e$  and  $\mu_v$ . In detail, the four thresholds for second-order tunneling marked by faint dotted lines in Fig. 2C are given by the conditions:  $\mu(0,1) = \mu_v$ ,  $\mu_e = \mu(0,1)$ ,  $\mu_e = \mu(0,2)$ , and  $\mu(1,1) = \mu_v$ . These second-order tunneling processes on their own generate a small current. Actually, similar processes are expected inside the  $N = 2$  and  $N = 3$  Coulomb blockade diamonds bound by solid lines in Fig. 2C, and indeed we see small current features inside these diamonds in Fig. 2B. We do not show the faint dotted lines for the  $N > 1$  diamonds in Fig. 2C simply to avoid complexity.
25. Referring to the forward bias potential diagram in Fig. 2A, we consider three possible second-order tunneling processes. Two of them involve elastic tunneling. The first is the case where the electron in dot 1 is virtually scattered to the  $2p$  state of dot 2 before it exits to the source. The second is the case where the electron in dot 2 virtually exits to the source followed by inter-dot tunneling of the electron in dot 1 to dot 2. The third process involves virtual spin exchange [i.e., the electron in dot 1 (dot 2) is scattered to the nearest contact lead, and an electron of opposite spin is simultaneously scattered back to dot 1 (dot 2) from the same contact lead]. In addition to these second-order tunneling processes, a small current can also be induced by spin flips inside the dot. This, for example, can arise from spin-orbit scattering; however, its contribution is not yet well understood (26).
26. T. Fujisawa *et al.*, *Nature*, in press.
27. L. P. Kouwenhoven *et al.*, *Science* **278**, 1788 (1997).
28. One might expect the resonance lines to be parallel to the vertical axis because the resonance condition is, in principle, fulfilled only by adjusting  $V$ . However, in practice, they are somewhat tilted because the resonance conditions are slightly modified by changing  $V_G$ . Note that these resonance lines terminate on the lowest-lying blue line in Fig. 2B (the threshold for electron tunneling from the drain to the lowest  $1s$  state of dot 1).
29. At high source-drain voltage beyond the  $1s$ - $2p$  resonance lines, other similar resonance lines are present. The evolution of these resonance lines with  $B$  field resembles very closely the familiar Fock-Darwin spectrum for single-particle states in a 2D harmonic potential (6, 30). Hence, we can straightforwardly assign these resonance lines with the  $3s$ ,  $3d$ , ... states in dot 2 (31).
30. T. Schmidt, R. J. Haug, K. von Klitzing, A. Förster, H. Lüth, *Phys. Rev. Lett.* **78**, 1544 (1997).
31. K. Ono, D. G. Austing, S. Tarucha, unpublished data.
32. C. Livermore, C. H. Crouch, R. M. Westervelt, K. L. Campman, A. C. Gossard, *Science* **274**, 1332 (1996).
33. We thank T. Fujisawa and M. Stopa for valuable discussions. K. O. and S. T. acknowledge financial support from the Specially Promoted Research, Grant-in-Aid for Scientific Research, from the Ministry of Education, Science, and Culture in Japan and from CREST-JST.

15 February 2002; accepted 16 July 2002

Published online 25 July 2002;

10.1126/science.1070958

Include this information when citing this paper.

# Probing Oxygen Motion in Disordered Anionic Conductors with $^{17}\text{O}$ and $^{51}\text{V}$ MAS NMR Spectroscopy

Namjun Kim and Clare P. Grey\*

Identification of the local environments of the ions in a solid-state electrolyte that contribute to the ionic conductivity or remain trapped in the lattice represents a challenge for many experimental probes of structure. We show that high-resolution  $^{17}\text{O}$  magic angle spinning nuclear magnetic resonance (MAS NMR) spectra may be obtained even from the highly disordered, layered materials  $\alpha\text{-Bi}_4\text{V}_2\text{O}_{11}$  and  $\gamma\text{-Bi}_4\text{V}_{1.7}\text{Ti}_{0.3}\text{O}_{10.85}$ , in which the different oxide sites in the lattice may be distinguished. The sites responsible for anionic conduction were determined directly from the variable-temperature  $^{17}\text{O}$  NMR spectra, and correlation times for motion were estimated. Double-resonance  $^{17}\text{O}/^{51}\text{V}$  NMR methods were used as confirmation of the assignments of the resonances and as a second experimental probe of motion that is sensitive to mobility involving oxide ion hops between the same crystallographic sites.

The ability to draw sufficient power from a fuel cell critically depends on the rate at which ions are transported across the membrane separating the two sources of fuel. For example, the  $\text{H}_2\text{-O}_2$  solid oxide fuel cell (SOFC) requires rapid oxide ion conduction across an oxide membrane (the electrolyte) (1). High oxygen ion conductivity is also essential for a quick response to changes in oxygen partial pressures in a solid-state oxygen sensor and for efficient oxygen separation with oxide membranes (2, 3). The material used commercially in SOFCs and sensors, yttria-stabilized zirconia, does not achieve a conductivity of  $10^{-2} \text{ S cm}^{-1}$  until

$700^\circ\text{C}$ ; thus the SOFCs and oxygen sensors are typically operated at temperatures of between  $900^\circ$  and  $1000^\circ\text{C}$  and  $500^\circ\text{C}$ , respectively (4).

The development and optimization of oxide conductors suitable for use at lower temperatures require an understanding of the mechanisms by which anions move in the solid and, thus, a determination of the oxygen sites that contribute to the conductivity and those that remain trapped in the solid. Solid-state nuclear magnetic resonance (NMR) can probe local structure and the local environments of the anions and cations in these inherently disordered materials. Although NMR is also sensitive to dynamics (5), it has not been widely applied to study oxide ion motion, in part because the low ionic conduction of most oxides has led to the consequent assumption that motion occurs on a much longer

time scale than that probed by magic angle spinning (MAS) NMR. Also, most standard MAS probes can only reach  $250^\circ\text{C}$ . High temperatures can be reached with a static probe but at the cost of the spectral resolution. Nonetheless, Adler *et al.* have used wideline and relaxation studies of oxygen mobility to estimate  $\text{O}^{2-}$  vacancy trapping energies and to investigate  $\text{O}^{2-}$  mobility at elevated temperatures (6, 7). Here, we extend our previously developed methodology for fluoride systems (8, 9) and report detailed  $^{17}\text{O}$  MAS NMR studies of oxide motion in the solid state. We show that a combination of  $^{17}\text{O}$  high-resolution MAS and  $^{17}\text{O}/^{51}\text{V}$  double-resonance [transfer of populations in double resonance (TRAPDOR)] (10, 11) NMR methods may be used to resolve the different crystallographic O sites, to determine which of these sites are responsible for conductivity, and to estimate the rates of exchange between sites.

A series of Aurivillius-type (12) oxides  $(\text{Bi}_2\text{O}_2)(\text{A}_{m-1}\text{B}_m\text{O}_{3m+1})$ ,  $\text{Bi}_4\text{V}_{2-x}\text{Me}_x\text{O}_{11-\delta}$  (where Me represents a large series of possible dopant cations), have been discovered that show moderate-to-high conductivities near ambient conditions (conductivities of  $10^{-4} \text{ S cm}^{-1}$  above  $200^\circ\text{C}$  for  $\text{Me} = \text{Ti}$ ) (1, 13–16). These materials can be used as oxygen separation membranes at moderate temperatures ( $430^\circ$  to  $600^\circ\text{C}$ ) (2). The idealized version of the structure of  $\text{Bi}_4\text{V}_2\text{O}_{11}$  is shown in Fig. 1 and consists of  $(\text{Bi}_2\text{O}_2)^{2+}$  and vanadium oxide perovskite layers. This represents a reasonable model for the high-temperature  $\gamma$  phase. A phase transition to the  $\beta$  phase occurs upon cooling to  $570^\circ\text{C}$ , where the vacancies in the perovskite layers partially order to form chains of alternating four- and five-coordinated V atoms (17). A further phase transition to the  $\alpha$  phase occurs at

Department of Chemistry, State University of New York at Stony Brook, Stony Brook, NY 11794–3400, USA.

\*To whom correspondence should be addressed. E-mail: cgrey@sbchem.sunysb.edu